

Contents

Congratulatory Message for the 60 th Anniversary of JEOL	2
Congratulations from Arizona State University	3
Marking Our 60th Anniversary	4
Aiming for Best Total Solutions	5
Exit Wavefunction Reconstruction	6
Single Shot Nanosecond Imaging in the Dynamic TEM	12
An Appraisal of High Resolution Scanning Electron Microscopy Applied To Porous Materials	17
Observation of Membrane Proteins Through An Electron Beam	23
HR-TEM of Carbon Networks - Towards Individual C-C Bond Imaging	32
Studies on Natural Antioxidant Derivatives: Enhanced Radical-Scavenging and Reduced Prooxidant Activities	38
Development of Nanoimprint Mold Using JBX-9300FS	46
Introduction of New Products	52

Cover micrograph

Restored phase of a 6-nm Pt particle obtained by applying spherical aberration correction and through-focus exit wavefunction restoration to a defocus series of 20 images acquired at 200 kV with the coefficient of spherical aberration, Cs, adjusted to -30 μm. (See page 9)
This micrograph is reproduced with permission from Angew. Chem. (Int. Ed.) Vol 46, p3683, 2007. Copyright Wiley-VCH Verlag GmbH & Co. KGaA.

Courtesy of Professor A. I. Kirkland, Department of Materials, University of Oxford.

[†]A. I. Kirkland and S. J. Haigh

Department of Materials, University of Oxford

Indirect methods for improving the resolution attainable in the TEM *via* image reconstruction of focal or beam-tilt series of images are now realising the promise they have long offered. This technique simultaneously recovers the complex specimen exit plane wavefunction and fully compensates for all measurable lens aberrations. Using an aberration corrected TEM and a tilt azimuth data acquisition geometry it can be shown that electron optical aberration correction and exit wave reconstruction enables the recovery of super resolved information beyond the axial information limit. In many cases the resolution improvement achievable is now limited by the sample and not by instrumental parameters.

Introduction

High Resolution Transmission Electron Microscopy (HRTEM) is now firmly established as one of the most important tools available for studies of the local microstructure and chemistry of a wide range of materials [1]. However, HRTEM records only the real valued image intensity, resolution limited by effects due to the partial spatial and temporal coherence of the illumination. This leads to an absolute information limit under axial illumination conditions of typically 100 times the wavelength for uncorrected instruments and 40 times the electron wavelength for the current generation of intermediate voltage corrected microscopes.

Indirect reconstruction of the complex wavefunction at the exit surface of the specimen (see [2] for a review) provides an attractive (but necessarily indirect) route to obtaining quantitative structural information with improved signal to noise characteristics at resolutions equal to or greater than those that can be achieved in conventional images.

The experimental datasets required for the successful implementation of this approach comprise several conventional HRTEM images recorded at either varying defocus levels [3-10] or with different illumination tilt directions [11-13]. Either of these acquisition geometries provides a set of differently aberrated images that contain independent information about the specimen exit plane wavefunction and the latter can subsequently be computationally recovered from the overde-

termined dataset. For this latter step, substantial progress has been made on the theoretical and computational problem of eliminating the non-linear image intensity components [4] and in the fully automated measurement of the aberration coefficients [14-16].

In 1997 initial results from TEM instruments fitted with electron optical elements designed for direct correction of otherwise unavoidable spherical aberration [17, 18] were announced. Commercial versions of these prototype instruments using an arrangement of sextupole elements and round lens transfer doublets have since been constructed, capable of direct correction of the coefficients in the wave aberration function to third-order and providing resolutions below 0.1nm at intermediate voltages. At the time of writing initial results from second-generation corrected electron optical systems capable of fifth-order correction have been reported [19, 20] targeting a resolution of 50 pm.

Focal and tilt series reconstruction methods have the advantage of recovering the fully complex specimen exit plane wavefunction, compensated for all measured objective lens aberrations. This data can also be retrieved using related approaches such as high resolution holography [21], diffractive imaging [22] and ptychography [23] in which a micro-diffraction pattern (from a very small area of the specimen) is recorded quasi-continuously as the illuminating probe scans the specimen. This additional data compared to that available in single HRTEM images allows structural inferences about the specimen to be made by comparison of experimentally recovered and simulated wave functions for trial structures with only one unknown experimental parameter (the specimen thickness). Thus, exit wavefunction restoration in all

[†]Parks Road, Oxford, OX110ES, UK.

Email: angus.kirkland@materials.ox.ac.uk



modes provides more quantitative structural information. Finally, as will be described subsequently there has been recent progress in combining electron optical correction and exit wavefunction reconstruction in which the former brings significant benefits to the resolution enhancement offered by the latter.

A Historical Overview

The first recorded reference to exit wavefunction reconstruction was provided by Schiske [24] although the use of tilted illumination in an optical analog was suggested as long ago as 1873 by Abbe [25]. However, successful experimental efforts were hampered until relatively recently by several factors. Firstly, at all resolutions the largely uninterpretable non-linear components of the image intensity, which increase with specimen thickness, required the development of new reconstructions algorithms [4]. Secondly, the largely uninterpretable image intensity arising from inelastically scattered electrons by any mechanism other than phonon scattering (which it should be noted do not affect Gabor holography) required the development of imaging filters [26-28]. Thirdly the range of directions and energies in the illuminating beam (formulated as the partial spatial and temporal coherence), imposes a resolution limit on the image signal more stringent than that due to the lens aberrations which required the development of new electron sources [29, 30]. Finally, the increased availability of CCD detectors for digital image recording has made it far easier to record the sets of images needed for wave function reconstruction [31, 32].

Field-emission electron sources provide much higher coherence levels than were previously available with thermionic emitters and have provided images with higher spatial frequencies, so that focal series reconstruction in particular achieves resolution significantly beyond the limit imposed by coherent objective lens aberrations. However, the price for this is a much wider point response, meaning heavy delocalisation of image detail, and making it essential to use comparatively

large field, high resolution electron detectors. The availability of these instrumental developments was utilised in the 1990s within a Brite Euram project that aimed to develop exit wavefunction reconstruction using both Gabor Holography and focal series datasets. The results from this provided the first experimental examples of exit wavefunction reconstructions at high resolution and also initiated the development of the paraboloid reconstruction method [6] which, although not optimal in its suppression of the non-linear imaging components provides useful physical insight into the reconstruction process.

Exit wavefunction reconstruction using tilted illumination requires that the primary beam is placed close to one side of an objective aperture. This allows it to interfere with beams scattered within the aperture at up to twice the maximum angle compared to the axial imaging mode, albeit eliminating beams scattered with different azimuths completely so that information must be combined from several images recorded with different tilt azimuths. However, for an optimum choice of tilt angle, the imaging properties of this mode compare favourably with those of the axial mode, and can achieve (in principle) a doubling of the resolution [12]. Since this approach synthesises a large effective Fourier space aperture from several smaller ones, it has also been termed 'aperture-synthesis' for comparison with similar established approaches in radio astronomy [33, 34] and radar [35]. Experimentally, exit wave reconstruction from tilt series datasets required the solution of two substantial technical problems in image analysis, *a posteriori* determination of the objective lens aberrations, including the beam tilt and mutual registration of differently aberrated images [11, 13] but was also demonstrated experimentally during the late 1990s [11, 13].

Outline Theory for Exit Wavefunction Reconstruction

The wave leaving an object for monochromatic, axial illumination can be separated into scattered and unscattered components as:

$$\Psi_o(\mathbf{x}) = 1 + \Psi_{so}(\mathbf{x}) \dots\dots\dots(1)$$

with the recorded image plane intensity given by:

$$I(\mathbf{x}) = |\Psi_{si}(\mathbf{x})|^2 = 1 + \Psi_{si}(\mathbf{x}) + \Psi_{si}^*(\mathbf{x}) + |\Psi_{si}(\mathbf{x})|^2 \dots(2)$$

Where $\Psi_{si}(\mathbf{x})$ is the electron wave in the real space image plane. If it is assumed that the scattering is sufficiently weak to ignore the quadratic term in (2) then the Fourier Transform of the image contrast is given as

$$c(\mathbf{k}) = \psi_{si}(\mathbf{k}) + \psi_{si}^*(-\mathbf{k}) \dots\dots\dots(3)$$

Where ψ_{si} is the electron wave in the Fourier space image plane and ψ_{si}^* it's complex conjugate. The Fourier transforms of the object and image waves are related by a wave aberration function $\gamma(k)$ and thus

$$\psi_{si}(\mathbf{k}) = \psi_{so}(\mathbf{k})w(\mathbf{k}) \dots\dots\dots(4)$$

where:

$$w(\mathbf{k}) = \exp\{-j\gamma(\mathbf{k})\} \dots\dots\dots(5)$$

Hence in terms of the object wave, $\psi_{so}(\mathbf{k})$, the Fourier Transform of the image contrast can be rewritten as

$$c(\mathbf{k}) = \psi_{so}(\mathbf{k})w(\mathbf{k}) + \psi_{so}^*(-\mathbf{k})w(-\mathbf{k}) + n(\mathbf{k}) \dots(6)$$

in which the term $n(\mathbf{k})$ represents the observed noise in the image.

All reconstructions now require an estimate, $\psi'_{so}(\mathbf{k})$ of $\psi_{so}(\mathbf{k})$ given a set of observed image contrast transforms, $c_i(\mathbf{k})$ and a knowledge of their individual transfer functions, $w_i(\mathbf{k})$. Therefore given data from several differently aberrated images, an *optimum* solution for $\psi'_{so}(\mathbf{k})$ can be defined in various ways [12]. In particular, a Wiener filter

applied to a focal or tilt series of images in the presence of noise gives an optimal estimate of the reconstructed wavefunction, expressed in the form of a weighted superposition of the image transforms as

$$\psi'_{so}(\mathbf{k}) = \sum_i \gamma_i(\mathbf{k}) c_i(\mathbf{k}) \quad \dots\dots\dots(7)$$

where, the *restoring filters*, $\gamma_i(\mathbf{k})$, depend on the complex wave transfer functions $w_i(\mathbf{k})$ for a set of images as

$$\gamma_i(\mathbf{k}) = \frac{W(-\mathbf{k})w_i^*(\mathbf{k}) - C^*(\mathbf{k})w_i(-\mathbf{k})}{W(-\mathbf{k})W(\mathbf{k}) - |C(\mathbf{k})|^2 + v(\mathbf{k})} \quad \dots\dots\dots(8)$$

$$W(\mathbf{k}) = \sum_i |w_i(\mathbf{k})|^2; C(\mathbf{k}) = \sum_i w_i(\mathbf{k})w_i(-\mathbf{k}) \quad \dots\dots(9)$$

For all the opacity of this expression, in the case of reconstruction using series of images the effect on a Fourier component transmitted by only a single image is simply to retain it after division by the corresponding transfer function, and for components present in all images to average the estimates obtainable from any pair of differently aberrated images. For a component not transferred in any image the value of the filter tends to zero due to the inclusion of the noise to object power ratio, $v(\mathbf{k})$. In the final step of the overall reconstruction process the exit-plane wavefunction itself is obtained simply by inverse transformation.

The approach to exit plane wavefunction restoration outlined above assumes linear imaging. Alternative methods have also been developed for the more general case, including the non-linear contributions to the image intensity. In the original implementation the non-linear image reconstruction was tackled by matching the electron wave to the measured intensities of images by minimization of a least squares functional (the multiple input maximum a posteriori, (MIMAP)). The improved, maximum likelihood (MAL) description [4] provides a computationally efficient, numerically optimized recursive solution and explicitly includes the coupling between the exit wave and its complex conjugate.

Experimental Exit Wavefunction Reconstruction

The theories outlined in the previous section can be applied equally to wavefunction reconstructions using either focal or tilt azimuth datasets. However these two geometries differ in their experimental advantages. In the case of a focal series reconstruction the use of a high coherence source to extend the microscope information limit is essential to maximise resolution enhancement. However, in the case of the tilt azimuth geometry it is the displacement of the transfer function envelope relative to the primary beam which is the essential element in achieving higher resolution, without explicitly requiring a high coherence source [11, 13]. The use of a high coherence source

still offers benefits to the latter geometry in the accurate determination of the imaging conditions and to date, all experimental restorations have utilised instruments fitted with field emission sources. However, overall, the tilt azimuth geometry is less sensitive to errors in the determination of the aberration coefficients and provides somewhat better recovery of low spatial frequencies. Set against these advantages image registration is simpler for focal series where the correlation peaks are centrosymmetric between all members of the dataset, which is not the case for images recorded at different illumination tilts. Finally, tilt azimuth reconstruction is potentially limited by parallax effects (see later) which are absent in focal series datasets, a factor that is ultimately limiting at extremely high resolution. As an early illustration of this approach, **Figure 1** shows the first reported example of a successful tilt series reconstruction in 1995 [11] using an uncorrected JEOL JEM-2010F in which the interpretable resolution has been

improved from 0.23 nm to 0.14 nm.

Exit Wavefunction Reconstruction with Aberration Corrected Images

Direct electron optical correction [17, 18] offers the advantage that it may be achieved on line in a single image, with no requirement for post acquisition processing or acquisition of extended focal or tilt azimuth series. However, for HRTEM imaging current generation electron optical correctors are only able to correct aberrations to third order in the wave aberration function with partial compensation of selected higher order terms for real recorded image data. Thus, for aberration corrected instruments computational reconstruction is still beneficial for both focal and tilt series data acquisition geometries as it both compensates for higher order terms and recovers the complex specimen exit surface wavefunction.

Indirect and direct correction / compensa-

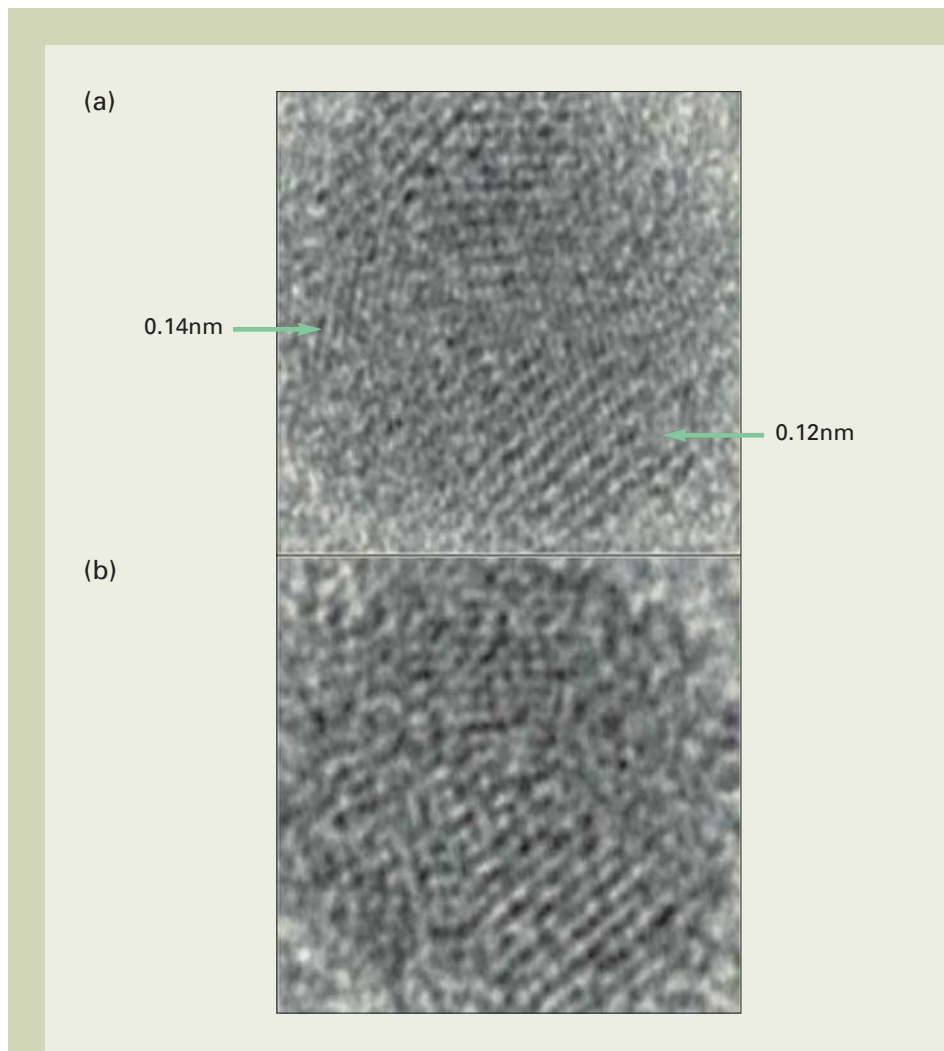


Fig. 1 (a) Modulus of the exit wavefunction of a gold nanoparticle reconstructed from a 4 member tilt series of uncorrected images with 0.14 and 0.12 nm fringes marked. (b) Original axial image recorded at the Scherzer defocus (200 kV, $C_s = 0.5$ mm).

tion have been used in combination [36, 37] and this provides additional advantages. For focal series datasets, the elimination of tilt-induced coma relaxes the requirement of using parallel illumination and enables the illumination to be converged onto the specimen area of interest. Thus, current density at the sample may be maintained while reducing the emitter current thereby giving a reduced energy spread in the illumination (for a Schottky source) and providing an improved information limit. For a tilt series dataset, the elimination of tilt induced axial coma gives rise to a less critical focus conditioning for any given tilt magnitude and multiple tilt magnitudes are also possible without a large induced focus change. For either data acquisition geometry, the reduced delocalisation of image components in electron optically corrected images is advantageous in quantitative interpretation. Finally, in aberration corrected instruments the voltage centre and axial coma free axis are coincident and hence the temporal coherence envelope is symmetric and

localized.

To illustrate the potential benefits from a combined direct / indirect approach to aberration correction and compensation **Figure 2** shows the phase of the specimen exit surface wavefunction of a Pt catalyst nanoparticle, viewed close to a $\langle 110 \rangle$ direction, reconstructed from a focal series of aberration corrected images acquired using a JEOL JEM-2200FS. Despite the presence of a graphitic carbon support, terraces and steps around the edge of the particle are visible and moreover, the visibility and spatial resolution within these features are improved significantly compared to a conventional HRTEM image. The monatomic steps that are visible in **Figure 2(a)** are conventionally termed *A* or *B* type, with either $\{100\}$ or $\{111\}$ microfacet atomic risers that have potentially different catalytic properties. Due to computational inversion of the HRTEM imaging process the heights of the peaks in the recovered phase are related to the number of atoms in each atomic column and can thus be used to obtain

information about the local atomic arrangement of each surface in cross section. Detailed examination of these provide evidence that the outermost atomic layers consist of irregular islands of atoms, in contrast to the atomic arrangements that have been proposed on the basis of homoepitaxial growth experiments on extended Pt surfaces [38].

Figure 3 emphasises the resolution improvement obtained by recovering the specimen exit wavefunction compared to that present in a single HRTEM image. The power spectra shown below each image in **Figure 3** clearly show the presence of higher-spatial resolution lattice fringe information in the reconstruction and equally importantly, the decreased contribution to the power spectrum from the quasi-amorphous carbon support.

Our next example demonstrates experimental verification of the resolution improvement possible using aberration corrected tilted illumination images. This requires a specimen with a real space lattice separation

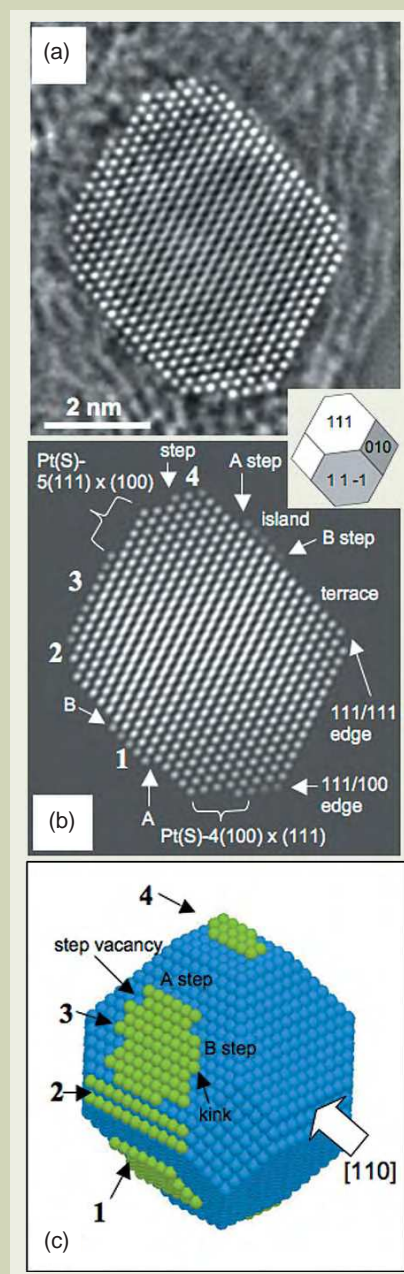


Fig. 2 (a) Phase of the reconstructed wavefunction of a 6-nm Pt particle obtained by applying spherical aberration correction and focal series exit wavefunction reconstruction to a dataset of 20 images acquired at 200 kV with a spherical aberration of $-30 \mu\text{m}$. (b) Best-fitting simulated phase. (c) Three-dimensional atomic model used to calculate the best-fitting phase in (b). The large white arrow indicates the direction of the electron beam. The inset overlapping parts shows the crystallographic details of the particle. In parts (b) and (c) labels 1-4 correspond to the same features on the surface of the particle. The notation $\text{Pt(S)-}n(x,y,z)\text{K}(u,v,w)$ refers to the microfacets, for which n is the number of atoms in the terrace, (x,y,z) is the Miller index of the terrace, and (u,v,w) is the Miller index of the step.

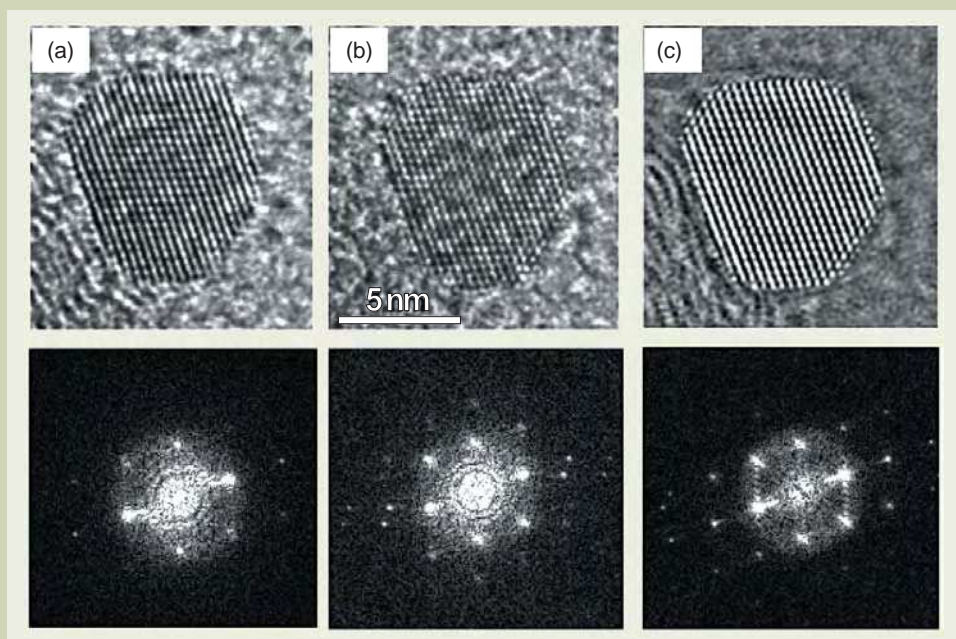


Fig. 3 (a) and (b) HRTEM (intensity) images of the Pt particle shown in **Fig 2(a)**, acquired with the spherical aberration adjusted to 0.5 nm (a) and $-30 \mu\text{m}$ (b). Corresponding power spectra are shown beneath each image. (c) Phase and power spectrum of the same particle, obtained by applying exit wavefunction reconstruction to a focal series of aberration corrected images.

beyond the axial information limit and a gold foil oriented along a $\langle 123 \rangle$ direction satisfies this requirement. **Figure 4** compares the phases and moduli of exit wavefunctions restored using both focal series and tilt defocus data sets. The only detail present in the phase and modulus of the exit wavefunction (Figures 4 (a) and (b)) recovered from the focal series dataset relates to the $\{111\}$ planes, which have a 0.235 nm lattice spacing. In contrast, the wavefunction recovered using tilted illumination data contains information at the positions of the $\{331\}$, $\{420\}$ and $\{242\}$ lattice reflections, corresponding to spacings of 0.093 nm, 0.091 nm and 0.083 nm which are beyond the 0.1 nm axial information limit of the microscope used.

As a final example we compare exit wavefunction reconstruction directly, now using focal and tilt series image datasets of images of thin crystals of $\langle 111 \rangle$ oriented SrTiO₃. **Figure 5** clearly shows the improvement in information transfer that can be obtained using a tilt-series data set for exit wavefunction reconstruction in which information transfer at 10% corresponding to a resolution of 0.12 nm is present for the focal series reconstruction, whereas the same level of information transfer limit is extended to 0.08 nm in the tilt-series reconstruction.

Although the data presented in this section clearly demonstrates that a combination of direct aberration correction and exit wave reconstruction is advantageous and moreover, that a tilt azimuth acquisition geometry enables super resolution, it is useful to examine in detail the limiting factors in this approach.

At large beam tilt magnitudes partial temporal coherence causes a loss of transfer at the centre of the tilted transfer function. For a beam tilt, $\tau_0 = \lambda \mathbf{k}_0$, beams at the same angle τ_0 with respect to the tilt axis are perfectly transferred and the temporal coherence envelope has no effect. However, for larger beam tilts the transfer falls away significantly inside this ring of perfect transfer (the achromatic circle). Reducing the tilt angle prevents this central transfer loss but reduces the resolution improvement compared to the axial case. This reduction in transfer for tilted illumination can in principle be recovered in the final reconstruction either by increasing the number of azimuthal angles or by including more than one tilt magnitude. However, either of these approaches increases the number of images required with consequent implications for experimental stability and overall radiation dose.

The second limiting factor is given by the variation within the experimentally measured axial aberration coefficients as a function of illumination tilt which can be estimated by taking the real part of the expansion of the wave aberration function with respect to the complex aberration coefficients and illumination tilt angle [39].

Finally, in contrast to exit wavefunction reconstruction using focal series data the individual images within a tilt series data set are not simply different measurements of the same projected specimen potential. Under tilted illumination the specimen potential is projected along a slightly different direction compared to the axial case and this introduces an additional phase shift in an image which can be estimated using a simple geometric parallax model. Choosing a maximum phase variation for a resolvable distance, d as $\pm\pi/2$, the maximum

parallax allowed between the top and bottom specimen surfaces relative to the middle of the specimen is $d/4$. For a beam tilt, τ , this leads to a maximum specimen thickness of $d/(2\tau)$. The simple geometric parallax argument described above is independent of the imaging conditions but has been found to be more stringent than the limit determined from a full dynamical calculation [40].

These various limits for wavefunction reconstruction using tilted illumination images are summarised in **Table 1**. This clearly demonstrates that the aperture synthesis approach to exit wavefunction reconstruction can use larger tilt magnitudes under aberration corrected imaging conditions, giving rise to the possibility of greater resolution improvement, significantly beyond the axial information limit of the microscope. However at very high resolution, parallax considerations become increasingly significant leading to a new regime where the sample limits the resolution attainable in tilt series exit wavefunction reconstruction.

Conclusions

In this paper we have highlighted the devel-

opment and application of exit wavefunction reconstruction in the TEM as a method for obtaining higher resolution, quantitative structural data using focal or more particularly, tilt azimuth series of images. We have also demonstrated the use of this technique in studies of nanocrystalline metal catalyst particles where local surface structures can now be described with atomic precision. Finally we have outlined the recent use of a combination of electron optical aberration correction and exit wavefunction reconstruction in a complimentary approach that further improves attainable resolution and have summarized the ultimate instrumental and specimen-based limitations to this.

Acknowledgment

It is a pleasure to contribute this paper to *JEOL News* on the occasion of JEOL's 60th anniversary. AIK would like to acknowledge Drs W. O. Saxton, R. R. Meyer, L. Y. Chang, H. Sawada, M. Kawasaki, K. Tsuno and F. Hosokawa for their substantial contributions to the development of exit wavefunction reconstruction and aberration measurement. We

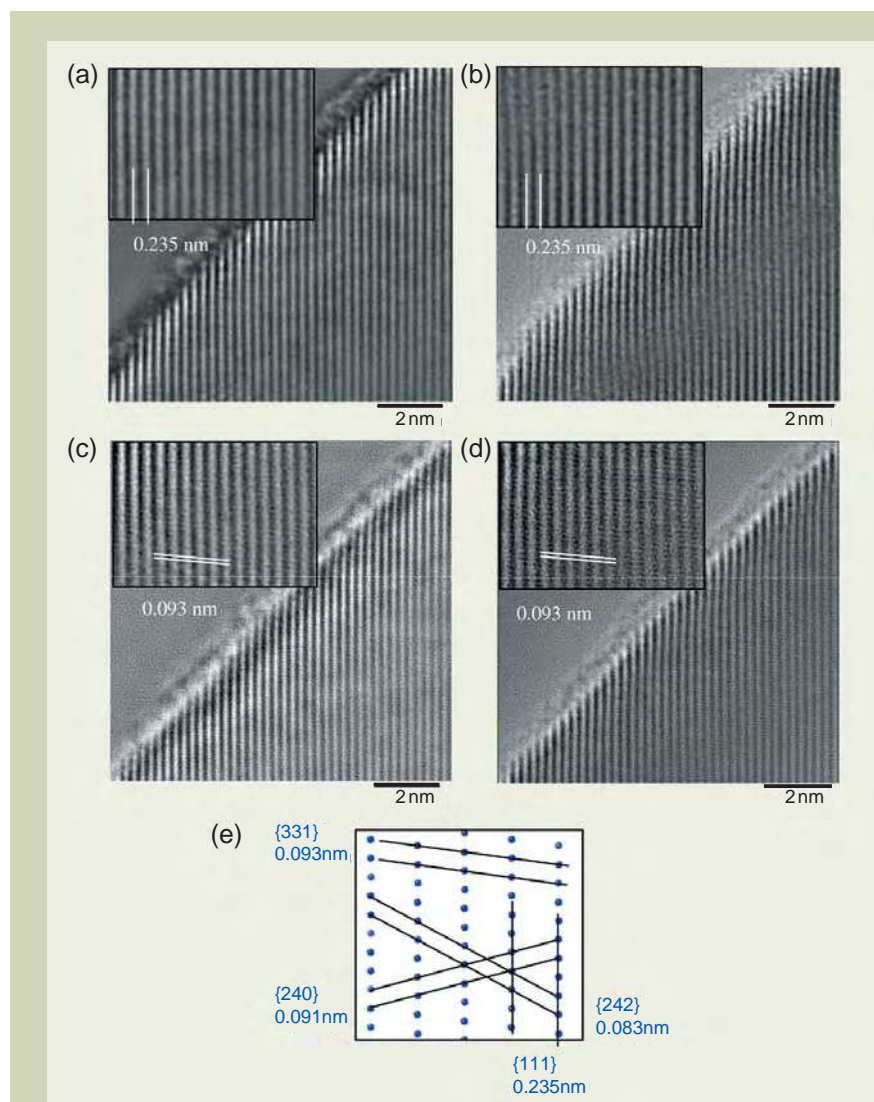


Fig. 4 Exit wavefunctions recovered from a gold foil oriented along a $\langle 123 \rangle$ direction. (a) and (b) phase and modulus restored using a 16 image focal series with a focal step of 7 nm. (c) and (d) phase and modulus of the same specimen area restored from a 27 image tilt-defocus data set with a maximum tilt magnitude of 18.4 mrad. (e) The atomic structure of gold projected along a $\langle 123 \rangle$ direction with lattice planes indicated.

would also like to acknowledge Dr Y Harada and M Hepburn from JEOL Ltd. and JEOL UK Ltd. respectively, together with other colleagues from these organisations for their continued enthusiastic support of research in advanced electron microscopy at Oxford.

References

[1] A. I. Kirkland, J. L. Hutchison Chapter 1 (pp3-64) in 'The Science of Microscopy' Eds. P. W. Hawkes and J. Spence, Kluwer Press, 2007 (2nd edition 2009).
 [2] A. I. Kirkland, R. R. Meyer, L. Y. Chang, *Microscopy and Microanalysis*, **12**(6), 461, (2006)
 [3] W. Coene, G. Janssen, M. Op de Beeck, D. van Dyck, *Phys. Rev. Letts* **69**, 3743, (1992)
 [4] W. M. J. Coene, A. Thust, M. Op de Beeck and D. van Dyck, *Ultramicroscopy*, **64**, 109, (1996)
 [5] D. van Dyck and M. Op de Beeck, *Ultramicroscopy*, **55**, 435, (1994)
 [6] M. Op de Beeck, D. van Dyck and W. Coene, *Ultramicroscopy* **64**, 167, (1996)
 [7] D. van Dyck D. and W. Coene,

Ultramicroscopy **15**, 29, (1984)
 [8] A. Thust, W. Coene, M. Op de Beeck and D. van Dyck, *Ultramicroscopy*, **64**, 211, (1996)
 [9] A. Thust, M. Overwijk, W. Coene and M. Lentzen *Ultramicroscopy*, **64**, 249, (1996)
 [10] M. Lentzen, B. Jahnen, C. L. Jia, A. Thust, K. Tillmann and K. Urban, *Ultramicroscopy*, **92**, 233, (2002)
 [11] A. I. Kirkland, W. O. Saxton, K. L. Chau, K. Tsuno, M. Kawasaki, *Ultramicroscopy*, **57**, 355, (1995)
 [12] W. O. Saxton. (pp213) in "Image and Signal Processing in Electron Microscopy, Proc. 6th Pfferkorn Conf., Niagara", Scanning Microscopy International Eds. P. W. Hawkes, F. P. Ottensmeyer, W. O. Saxton and A. Rosenfeld A., (1988)
 [13] A. I. Kirkland, W. O. Saxton and G. Chand, *J. Electron Microscopy*, **1**, 11, (1997)
 [14] F. Zemlin, K. Weiss, P. Schiske, W. Kunath and K. H. Herrmann, *Ultramicroscopy*, **3**, 49, (1978)
 [15] R. R. Meyer, A. I. Kirkland and W. O. Saxton, *Ultramicroscopy*, **92**, 89, (2002)

[16] R. R. Meyer, A. I. Kirkland and W. O. Saxton, *Ultramicroscopy*, **99**, 115, (2004)
 [17] M. Haider, H. Rose, S. Uhlemann, B. Kabius and K. Urban, *Nature* **392**, 768, (1998)
 [18] M. Haider, H. Rose, S. Uhlemann, B. Kabius and K. Urban, *J. Electron Microsc.* **47**, 395, (1998)
 [19] C. Kisielowski, B. Freitag, M. Bischoff, H. van Lin, S. Lazar, G. Knippels, P. Tiemeijer, M. van der Stam, S. von Harrach, M. Stekelenburg, M. Haider, H. Muller, P. Hartel, B. Kabius, D. Miller, I. Petrov, E. Olson, T. Donchev, E. A. Kenik, A. Lupini, J. Bentley, S. Pennycook, A. M. Minor, A. K. Schmid, T. Duden, V. Radmilovic, Q. Ramasse, R. Erni, M. Watanabe, E. Stach, P. Denes, U. Dahmen, *Microscopy and Microanalysis* **14**, 454, (2008)
 [20] H. Sawada, F. Hosokawa, T. Kaneyama, T. Ishizawa, M. Terao, M. Kawazoe, T. Sannomiya, T. Tomita, Y. Kondo, T. Tanaka, Y. Oshima, Y. Tanishiro, N. Yamamoto and K. Takayanagi, *Jpn. J. Appl. Phys.* **46**, L568-L570, (2007)
 [21] M. Lehmann, H. Lichte, D. Geiger, G. Lang and E. Schweda, *Materials Characterisation*, **42**, 249, (1999)
 [22] J. M. Zuo, I. Vartanyants, M. Gao, R. Zhang, L. A. Nagahara, *Science*, **300**, 1419, (2003)
 [23] P. D. Nellist, B. C. McCallum and J. M. Rodenburg, *Nature* **374**, 630, (1995)
 [24] P. Schiske (pp82) "Image Processing and Computer Aided Design in Electron Optics", Ed. P. Hawkes, London: Academic Press, (1973)
 [25] E. Abbe, *Arkiv Mikroskopische Anat.*, **9**, 413, (1873)
 [26] O. L. Krivanek, A. J. Gubbens, N. Dellby and C. E. Meyer, *Microsc. Microanal. Microstruct.* **3**, 187, (1992)
 [27] H. Rose and E. Plies E, *Optik*, **40**, 336, (1974)
 [28] K. Tsuno, T. Kaneyama, T. Honda, K. Tsuda, M. Terauchi and M. Tanaka, *J. Electron Microscopy*, **46**, 357, (1997)
 [29] M. T. Otten and W. M. J. Coene, *Ultramicroscopy*, **48**, 77, 1993.
 [30] T. Honda, T. Tomita, T. Kaneyama and Y. Ishida, *Ultramicroscopy*, **54**, 132, (1994)
 [31] J. Spence and J. Zuo, *Rev. Sci. Inst.* **59**, 2102, (1988)
 [32] R. R. Meyer, A. I. Kirkland, R.E. Dunin-Borkowski, J. L. Hutchison, *Ultramicroscopy*, **85**, 9, (2000)
 [33] F. G. Pease, *Ergeb. Exakt. Naturwiss.* **10**, 84, (1931)
 [34] A. A. Michelson, *Phil. Mag.* **30**, 1, (1890)
 [35] M. Ryle and D. Vonberg, *Nature* **158**, 339, (1946)
 [36] L. Houben, A. Thust, K. Urban *Ultramicroscopy*, **106**, 200, (2006)
 [37] L. Cervera Gontard, L.-Y. Chang, C. J. D. Hetherington, A. I. Kirkland, D. Ozkaya, and R. E. Dunin-Borkowski, *Angew. Chem.*, **46**, 3683, (2007)
 [38] B. Lang, R. W. Joyner, G. A. Somorjai, *Surf. Sci.* **30**, 454, (1972)
 [39] A. I. Kirkland, S. J. Haigh, H. Sawada, *Phil. Trans. Proc Roy. Soc*, in press (2009)
 [40] R. R. Meyer, PhD Thesis, Dresden University, (2002)

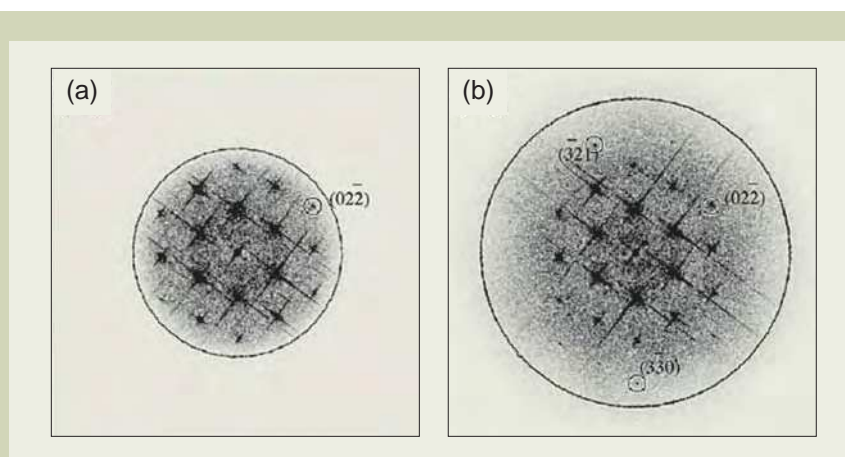


Fig. 5 Moduli of Fourier transforms of the complex specimen exit wavefunctions of $\langle 111 \rangle$ -oriented SrTiO_3 reconstructed using (a) focal-series data and (a) combined tilt/focal-series data. Circles indicate the limit for which information transfer drops below 10%, equivalent to a spatial resolution of 0.12 nm for the focal series and 0.08 nm for the tilted data set. Selected high-order reflections are highlighted to emphasize the presence of additional information in the exit wavefunction recovered from the tilt/focal-series data compared to the axial focal series data. Experimental focal series comprised 20 images separated by a focal increment of 10 nm with the series centered at the Gaussian focus with a spherical aberration of $-3 \mu\text{m}$. Tilt series consisted of six short focal series taken at different illumination tilt directions using tilt magnitudes of up to 20 mrad.

Table 1 Tilt limits determined for an object thickness of 2 nm at 200 kV assuming third order aberration correction and a focal spread = 4 nm.

Limiting Factor	Maximum Tilt Magnitude	Resolution Limit
Incoherent Aberrations	19 mrad	0.0629 nm
Coherent Aberrations	25 mrad	0.0547 nm
Geometric Parallax	18 mrad	0.0645 nm